Journal of Materials Research and Technology 42 (2026) 4648–4656

Contents lists available at ScienceDirect

Journal of Materials Research and Technology

journal homepage: www.elsevier.com/locate/jmrt

Protective laser cladding coatings for thermal energy storage tanks in contact with molten salt-based nanofluids

Lorena Betancor-Cazorla, Adela Svobodova-Sedlackova, Genís Clavé, Camila Barreneche *, Sergi Dosta **

Departament de Ciència de Materials i Química Física, Universitat de Barcelona, C/Martí i Franqués 1, 08028, Barcelona, Spain

ARTICLE INFO

Keywords:
Laser cladding
Coatings
Corrosion
Thermal energy storage (TES)
Concentrating solar power (CSP)
Molten salt
Nanofluids

ABSTRACT

Intermittency of renewable energy sources is a critical problem. Concentrated Solar Power (CSP) power plants with thermal storage systems offer one of the main solutions. Among the many storage processes, nanofluids are a method of improving thermal performance but inducing corrosion of storage units. This study investigates the potential of Inconel-625 and Stellite-6 coatings deposited by laser cladding in preventing nanofluid-induced corrosion in CSP thermal storage units. AISI 316L stainless steel samples coated with Stellite-6 and Inconel-625 were tested for corrosion in $NaNO_3$ containing SiO_2 nanoparticles at 450 °C for 30, 60, and 90 days. Cross-section analysis was used to assess thickness loss, and coatings were analysed. Chemical attack enhanced material contrast for microstructural observation. Compositions of oxides were identified by EDS and XRD analysis, and ICP analysis identified elements in the salts after corrosion. Results showed almost no loss in thickness, even after 90 days, to substantiate the protective efficacy of coatings. Results confirm that Inconel-625 and Stellite-6 coatings are a reliable source of preventing corrosion caused by nanofluids in CSP thermal storage systems.

1. Introduction

The contribution of renewable energies to primary energy consumption has been increasing exponentially over the last few years [1]. This is mainly due to the fact that they are an effective solution to achieve sustainable and environmentally friendly development. Likewise, they allow a balance to be achieved between social and economic welfare. However, this growth has introduced the challenge of intermittency in energy production. As a result, new technologies and systems began to be developed to manage and store this energy efficiently [2]. A wide variety of materials have been investigated for energy storage applications, ranging from functional ceramics and magnetic materials to molten salts and nanofluids, depending on the targeted storage mechanism and operating conditions [3]. In this context, Concentrating Solar Power (CSP) plants equipped with Thermal Energy Storage (TES) systems have emerged as a promising alternative. These systems offer several advantages (e.g., flexibility, €/kWh_{th} reduction, and minimising dependence on fossil fuels), enabling the transition to renewable energy sources [4,5], and the usage of coating engineering is a key factor in improving the energy performance of molten salt-TES systems [6] as stated by Dosta et al.

This technology consists of different materials, including concrete, solid beds, and molten salts as TES material and/or heat transfer fluid HTF [7,8]. Using these materials, sensible heat is stored and subsequently used to produce electricity, ensuring continuous electricity generation [9]. Consequently, the materials used in these systems required high thermo-physical properties and chemical stability to obtain an efficient storage system.

CSP's most mature and implemented technology is a two-tank TES storage system with molten salts, especially with the so-called solar salt, composed of 60 wt% sodium nitrate ($NaNO_3$) and 40 wt% potassium nitrate (KNO_3). Despite the good performance of molten salts as TES material, some critical drawbacks remain to be solved. One of the most relevant is the high corrosion rates of molten salts working at high temperatures on the metallic walls of the storage tanks [10,11]. The high reactivity of these salts at high temperatures allows the reaction with the tank metals, producing severe oxidation and corrosion. However, despite extensive research, these corrosion degradation mechanisms are

* Corresponding author.
** Corresponding author.
E-mail addresses: c.barreneche@ub.edu (C. Barreneche), sdosta@ub.edu (S. Dosta).

https://doi.org/10.1016/j.jmrt.2026.04.038
Received 15 May 2025; Received in revised form 4 February 2026; Accepted 5 April 2026
Available online 6 April 2026

not fully understood. Multiple factors, such as tank design, materials used, start-up, and operating conditions, play an important role in the evolution of these mechanisms [12]. Finding a solution to reduce this corrosion is therefore critical to improving CSP plant efficiency and the durability of TES systems.

On the other hand, molten salts exhibit a relatively low specific heat capacity (c_p) and low-temperature stability, limiting the storage efficiency. In this regard, in recent years, research on the potential use of molten salt-based nanofluids has been carried out [13–15]. Nanofluids are a stable colloidal suspension of low concentrations of nanoparticles in molten salts. The literature indicates that the addition of around 1 wt % of nanoparticles increases the specific heat capacity and enhances the temperature stability. Consequently, enhancing the energy density of the system [16–19] and the Brayton cycle [20]. Furthermore, there are studies in the literature that demonstrate the reduction of corrosive behaviour due to the incorporation of nanoparticles in molten salts [21, 22]. These nanoparticles tend to aggregate and can be incorporated into the formed surface oxide layer, reducing the growth of it. However, there are other studies that indicate the opposite, showing an increase in the corrosion rate due to their presence [23]. Although the exact behaviour of nanoparticles and their effects on storage materials are not known, their role is important in future research in the field of CSP plants.

Within this framework, coatings are an effective solution to address this issue, safeguarding material from corrosion. Laser cladding has become an innovative option among the different methods of applying these protective layers [24]. This technique is widely used in the petrochemical, aerospace, and automotive industries due to its flexibility in terms of materials and structure [24,25]. It also stands out from other types of deposition technologies [26] because it enables a complete metallurgical bond with minimal heat input to the substrate [27]. Furthermore, manipulation of the laser parameters and post-treatments, such as controlled cooling or reheating, has been shown to have a tangible impact on the coating properties [28,29]. This highlights the importance of controlling the process parameters for optimum corrosion protection properties [30].

Among the different materials, nickel (Ni) and cobalt (Co) base alloys, such as Inconel and Stellite, have shown outstanding corrosion resistance, especially when applied using thermal spraying or laser cladding techniques [28,31–36]. However, most existing studies have been conducted in corrosive media at room temperature, such as HCl or NaCl solutions [31,37–39], which are not representative of conditions in CSP plants. However, more recent research has evaluated the behaviour of these alloys in molten salts at high temperatures, such as mixtures of nitrates and eutectic salts [40–44], demonstrating their potential as a barrier against corrosion in harsh environments. For this reason, this work intends to analyse the effectiveness of these coatings deposited by the laser cladding technique.

The main objective of this paper is to evaluate the effectiveness of Inconel-625 and Stellite-6 coatings, applied by laser cladding, to mitigate and prevent nanofluid-induced corrosion in thermal energy storage (TES) systems. This evaluation includes the study of their performance against corrosion over different periods of time, combined with a detailed analysis of the coatings' microstructural characteristics to assess their feasibility and efficiency.

2. Materials, methods, and experimental procedures

2.1. Molten salt-based nanofluids synthesis

The molten salt-based nanofluids (Fig. 1) were synthesised using commercial Sodium Nitrate ($NaNO_3$) (Sigma Aldrich, 99.995%) as the base fluid and 1 wt% of silica nanoparticles (SiO_2 NPs) ranging in diameter from 5 to 15 nm (Sigma Aldrich, 99.5%). The synthesis followed a standard two-step method [45] involving the following steps [46].

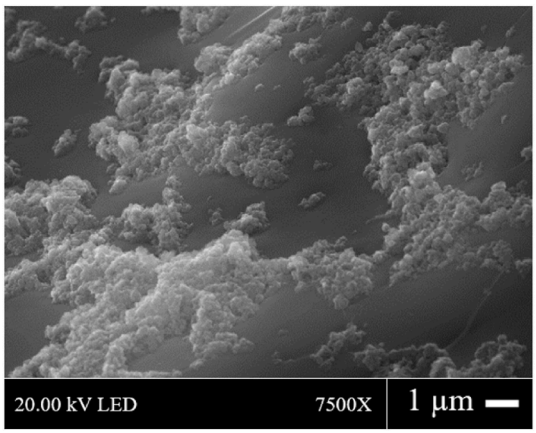

Fig. 1. Molten salt-based nanofluid SEM image (7500X, 20 kV).

1. Preparing an 80 g sample by weighing 1 wt% SiO_2 NPs and complete with $NaNO_3$ until the desired weight is reached.
2. Dissolve the mixture in 30 ml of distilled water.
3. Subjecting the solution to 30 min of sonication to ensure proper dispersion of the nanoparticles and homogenization of the nanofluid.
4. Drying the solution in a furnace at 105 °C until complete water evaporation and salt recrystallisation.
5. Grinding the resulting material in an Agate mortar.

This method ensured the formation of the desired molten salt-based nanofluids with well-dispersed silica nanoparticles uniformly integrated into the solution.

2.2. Corrosion test materials

The specimens tested are comprised of AISI 316L stainless steel, the most common stainless steel used in TES tanks [47]. This substrate has been layered with laser cladding coatings of Inconel-625 and Stellite-6 developed by the Spanish company TMCOMAS. Detailed compositions for both powder coating materials are provided in Tables 1 and 2 for reference and analysis. Both powders present a spherical morphology and a particle size of −150 + 53 µm, as shown in Fig. 2.

2.3. Laser cladding technique

The Inconel-625 and Stellite-6 coatings were deposited by laser cladding according to the optimum conditions of TMCOMAS as shown in the following Table 3.

Multiple tracks were applied in this study, each measuring around 900 µm, and three tracks were applied. A post-machining was performed on the coatings to reduce their roughness.

2.4. Experimental procedure corrosion test

The corrosion test involves immersing the samples in molten salts-based nanofluids contained within alumina crucibles and maintaining them at 450 °C in an air atmosphere for durations of 30 days (720 h), 60 days (1440 h) and 90 days (2160 h) in a muffle furnace. Specifically, eight samples were under testing: three coated with Inconel-625 for each period of time duration and three coated with Stellite-6 for each period.

Table 1
Inconel-625 powder chemical composition.

Composition (wt.%)				
Ni	Cr	Mo	Nb/Ta	Fe
61.7-68.1	20.0-23.0	8.0-10.0	3.2-3.9	0.8-1.5

Table 2
Stellite-6 powder chemical composition.

Composition (wt.%)					
Co	Cr	W	Fe	Si	C
60.2-66.4	27.5-29.5	4.0-4.8	0.3-3.0	0.9-1.3	0.9-1.2

Samples of 316 L stainless steel were also tested to evaluate the independent performance of this material for durations of 30 days and 90 days. To exclusively perform a corrosion test on one side of the samples, the remaining sides were protected with a thermal paste (Nural 30 from Pattex).

2.5. Characterization methods

The cross-section of the samples was cut using an ABRASIMENT 250 machine with a 60A25 abrasive disc. The cut samples were embedded in resin using a hot mounting press machine (REMET - IPA 30 EVOLUTION). The samples were then roughed down and polished. To evaluate the microstructure of the samples, Marble attack reagent was prepared from 2 g of copper sulphate ($CuSO_4$), 10 ml of hydrochloric acid (HCl 37%), and 10 ml of distilled water. Once prepared, the samples were immersed in the attack reagent for 4 s.

Scanning Electron Microscopy was applied to see the morphology of the samples and the coatings. The equipment used was a QUANTA 200 SEM microscope with EDS (Energy Dispersive X-Ray). The evaluation of the oxide layers and free surface of the samples was analysed, and the chemical analysis of Inconel-625 and Stellite-6 powders was carried out by the EDS. FESEM JEDL J-7100 microscope (GATAN MONO-CL4 cathodoluminescence spectrometer, EDS detector, backscattered electron detector) was used for salt micrographs. In addition, mappings of the cross-section of the coatings were performed to study the formation of oxides after the corrosion test.

X-ray diffraction (XRD) test was performed with PANalytical X'Pert PRO MPD, Bragg-Brentano powder diffractometer with 240 mm radius with Co $K\alpha$ radiation. Six samples were analysed: Stellite-6 powder, Inconel-625 powder, one sample of Inconel-625, and one of Stellite-6 before the test and one sample of each after the corrosion test (90 days). The measurements were obtained in continuous scan mode between the 2θ range from 7° to 125° with a step size of 0.017° and a measuring time of 100 s per step.

Inductively Coupled Plasma Atomic Emission Spectroscopy (ICPAES) and Inductively Coupled Plasma Mass Spectrometry (ICP-MS) was performed to detect and identify the metal elements present in the samples' composition. 100 mg samples were mixed with 1 ml of nitric acid (HNO_3) and 1 ml of hydrofluoric acid (HF), for 24 h in an oven at 90 °C. After the 24h, 45 ml H_2O (high purity) were added to the mixture for 12h at 90 °C. The samples were analysed in two steps; the first step involved using the ICP-AES technique, which was performed on PerkinElmer ELAN 6000 ICP mass spectrometer to analyse Si content. In the second step the ICP-MS was employed to analyse chromium (Cr), molybdenum (Mo), cobalt (Co), tungsten (W) and nickel (Ni) based on the detection limit of the technique, and an ICP-OES simultaneous PerkinElmer Optima 3200R spectrometer was used to analyse these elements. Two measurements were taken for each sample.

3. Results and discussion

After the immersion corrosion test in molten salt-based nanofluids, none of the samples showed significant signs of surface corrosion. The coated samples, after 90 days, remain without apparent cracks (Fig. 3). This was mainly due to this technique's ability to create compact, low porosity (lower than 2% porosity), obtaining dense and uniform coatings, which reduces their susceptibility to corrosion [28].

Also, the coating is perfectly adhered to the substrate and has a wide thickness that protects it from the corrosive behaviour of the nanofluids and increases its service life (Fig. 4). Generally, this technique needs high cooling rates which limits the layer thickness to 500 μm [48]. However, in this case, the coating layers obtained are between 2000 and 3000 μm. This means that during cooling, stresses can be generated at the interface and cause cracks in the coating, allowing the corrosion path [49]. Nevertheless, the thickness obtained prevents this phenomenon to happen.

In the case of the coated samples, the thickness variation (Δthickness) in μm produced after performing the test for 30, 60 and 90 days was analysed. As the laser cladding technique produces irregular zones in the contact area between substrate and coating, to calculate the coating thickness, a measurement criterion was established from the surface to the tangent to the curves due to the laser trajectory. This reduced the error in thickness measurements caused by this irregularity. For both Inconel-625 and Stellite-6 samples, the variation observed for the first two months is insignificant. However, for the 3-month period, 30.2 ± 6 μm for Inconel-625 and 26.9 ± 10 μm for Stellite-6 values were obtained (Fig. 5). This translated into reduction percentages of 1.2 ± 0.2% and 0.8 ± 0.3%, respectively. Furthermore, the corrosion rate (μm/year) was calculated from the coating thickness losses. Thus, after 3

Table 3
Laser deposition parameters of Inconel-625 and Stellite-6 (power, mass flow rate, and velocity).

Powder material	Power (W)	Mass flow rate (g/min)	Velocity (mm/min)
Inconel-625	3400-3700	27-35	1200-1400
Stellite-6	3400-3700	25-30	800-1100

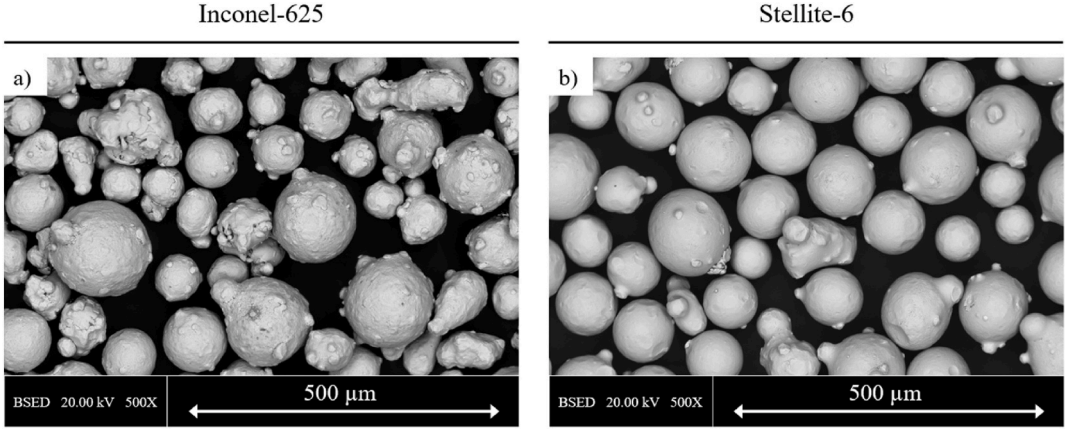

Fig. 2. Powder materials SEM images: a) Inconel-625 powder and b) Stellite-6 powder scanning electron image (500X, 20 kV).

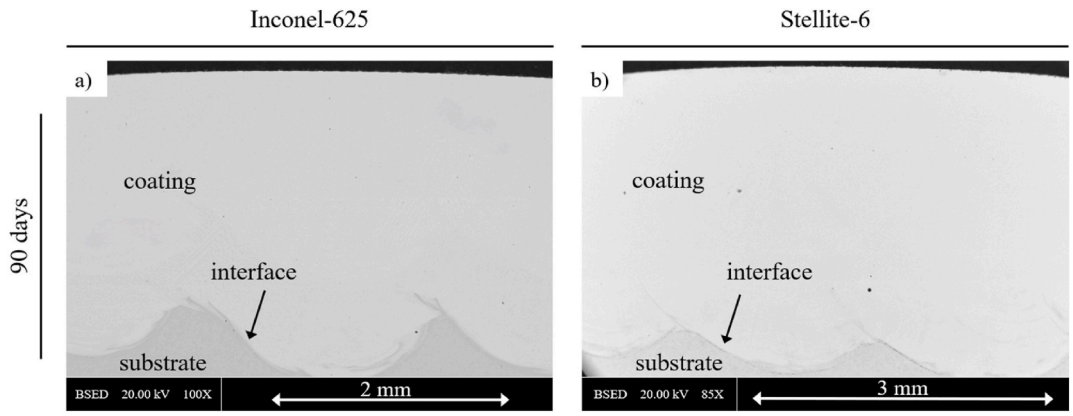

Fig. 3. SEM images of the samples after 90 days of testing: a) Inconel-625 and b) Stellite-6.

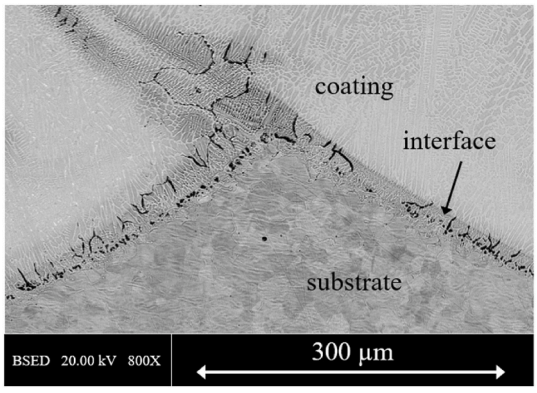

Fig. 4. Image SEM of the substrate-coating (Stellite-6) bonding zone.

months of testing, Inconel-625 reaches a corrosion rate of 122.5 ± 24 µm/year and Stellite-6 of 109.2 ± 40 µm/year. For better comparison,

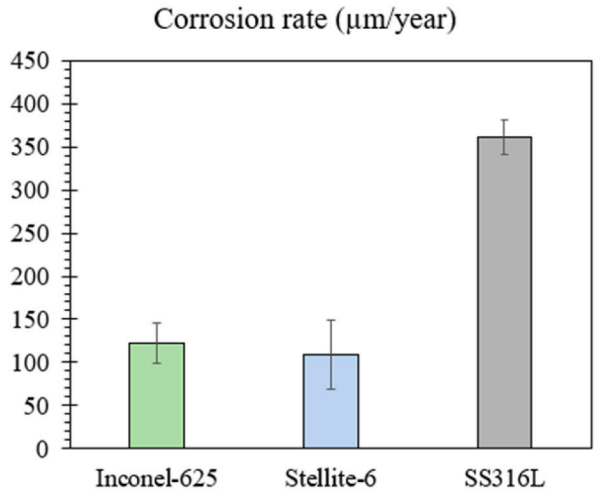

Sample	Δthickness (µm)
Inconel-625	30.2 ± 6
Stellite-6	26.9 ± 10
SS316L	89 ± 5

Fig. 5. Corrosion rate (µm/year) for Inconel-625 (green), Stellite-6 (blue) and SS316L (grey), and thickness reduction after 3 months.

the corrosion rate of 316L stainless steel was estimated for 30 and 90 days of exposure to molten salt-based nanofluids. This value was calculated from the reduction in material thickness. Thus, the area covered by the oxide layer formed was eliminated. Thus, after 90 days, a reduction in thickness of 89 ± 5 µm was achieved. This implied that the corrosion rate of this material reached 361.1 ± 20 µm, a speed much higher than that observed for stainless steel coated with Inconel-125 and Stellite-6. Therefore, using coatings can reduce the corrosion rate of the material in the range of 65-70%.

Corrosion due to the high temperatures of molten nitrates in structural materials in TES applications has been extensively studied over the years. It is therefore widely known that steels tend to form layers rich in iron oxides that are significantly higher than those of Ni- and Co-based superalloys. Specifically, for the substrate material used (SS 316L), although there is no direct experimental data in pure $NaNO_3$, there are several studies [50–54] in solar salt and $NaNO_3$-based molten salts that report data close to 0.01 mm/year, which depend on the test conditions (salt purity, atmosphere, and test time) and the method used to calculate the corrosion rate. That is why results obtained using different calculation methods cannot be used to make a true comparison of the behaviour of the material, and for this reason, the same calculation method has been used for coatings and substrates in this study.

In the case of studies on Inconel and Stellite in molten salts, something similar occurs, as no direct studies are using these coatings under the same test conditions. In general, Inconel 625 performs well against corrosion and has been extensively studied in solar salt. From the bulk material itself, where static and dynamic test conditions at 600 °C in solar salt resulted in values of 17-26 µm/year [40,55], to coatings of this material, which proved to be more effective with results of 13 µm/year [56]. Furthermore, the performance of Inconel 625 laser cladding coatings is supported by their extensive use in other types of more corrosive salts. Naghiyan et al. [57] studied Inconel 625 deposited on Inconel 738 in Na_2SO_4-60 wt%V_2O_5 at 900 °C and discovered the formation of a 40 µm layer after 36 h, significantly lower than the 130 µm layer of the substrate material under the same conditions. Meanwhile, Wang et al. [58] deposited Inconel 625 onto Q245R boiler steel using high-speed laser cladding and subjected it to a test in 33% NaCl + 31% KCl + 9% Na_2SO_4 + 27% K_2SO_4 mixed salt (400-600 °C). The results showed good corrosion resistance, which deteriorates as the temperature rises and causes cracking and pitting corrosion. In contrast, Stellite 6 is not a material commonly used in molten salt testing. An important study in this area is that of Sidhu et al. [33] in Na_2SO_4–60%V_2O_5 at 900 °C under cyclic conditions, where Stellite 6 coating was found beneficial in increasing the resistance to hot corrosion. The most noteworthy studies are those on its resistance to wear and corrosion (3.5% NaCl solution) for applications involving high temperatures (e.g. high-pressure steam valves, oil or petrochemical industry) [59–61].

This corrosion originates mainly due to the sodium nitrate decom-

position releases nitrogen oxides (e.g., NO_2) and oxygen (O_2) (Equation (1)). This free oxygen mainly causes the oxidation of iron, present in steels and alloys, towards the form of higher stability, magnetite (Equations 2 and 3) [62]. In addition to magnetite, the formation of other iron oxide phases, such as Fe_2O_3, is possible. Also, impurities present in the molten salts can accelerate the corrosion process due to the presence of magnesium, chlorides, carbonates and sulphates [62,63]. This can result in the formation of different types of oxides and ternary compounds, depending on the material (stainless steel, alloys, or superalloys) introduced into the molten salt-based nanofluids.

$$NO_3^- \leftrightarrow 2NO_2^- + O_2 \quad (1)$$

$$2Fe + O_2 \leftrightarrow 2FeO \quad (2)$$

$$3FeO + \frac{1}{2}O_2 \leftrightarrow Fe_3O_4 \text{ (magnetite)} \quad (3)$$

In the test carried out, all the samples showed the formation of oxide layers on the surface (Fig. 6). The thickness of these increases as the exposure time in the nanofluids increases. These were studied from the cross-section of the samples and the analysis of the free surface of the specimens.

For the Inconel-625 samples, the oxide layer formed ranges from 6 μm to 11 μm (Fig. 6-a). Fig. 7-a shows the cross-section mapping, where the oxide layer formed is clearly appreciated. It was mainly composed of nickel (Ni) and chromium (Cr), which are essential elements in this superalloy. In addition, Mo accumulation could be observed in some areas of this layer. This is in agreement with test results of this material in different corrosive environments (solar salt, Na_2SO_4- 45 wt% Diatomite eutectic molten salt mixture) [40,41]. The presence of the nanoparticles was not observed at the cross-sectional level, which is in accordance with studies indicating that the nanoparticles do not affect the corrosion rate caused in Ni-based superalloys [23].

On the other hand, for the Stellite-6 samples, the oxide layer formed was smaller, in the range of 4 to 7 μm (Fig. 6-b). This confirms a better stability and excellent results in terms of corrosion resistance of this material. Some studies have attributed this behaviour to the absence of nickel (Ni), which tends to form nickel (II) oxide (NiO) on the surface of the coating [42]. Furthermore, in this case, Fig. 7-b shows the appearance of a solid layer composed of silicon and oxygen on the cross-sectional surface of the sample. However, in general, in the studies carried out with this coating in different corrosive environments, the oxides layer formed is based on cobalt and chromium oxides [43,64], since the element content in the material is high. This difference in the composition of the surface oxide layer may have been caused by the nanoparticles. The agglomeration of these on the coating surface, forming a homogeneous layer, could have prevented the corrosive attack of the salt and the formation of the expected oxides. Moreover, this behaviour was similar to the one observed in other studies [22,65], where the addition of nanoparticles has a positive effect on the decrease of the corrosion level, highlighting the tendency to agglomerate and incorporate into the oxide layer on the surface.

In comparing these results with the uncoated substrate material, it was observed that the oxide layer formed was significantly larger, reaching 50-70 μm after 3 months of testing (Fig. 6-c). The layer formed is constituted by different particles of several compositions (silicon [Si], aluminium [Al], iron [Fe], nickel [Ni]). Other elements, such as sodium and magnesium, were also observed in smaller proportions. These results are in concordance with other studies that evaluate the performance of stainless steels in solar salt [62].

The thickness loss results showed relatively uniform degradation of the coatings after 90 days of exposure to molten salt nanofluids. This

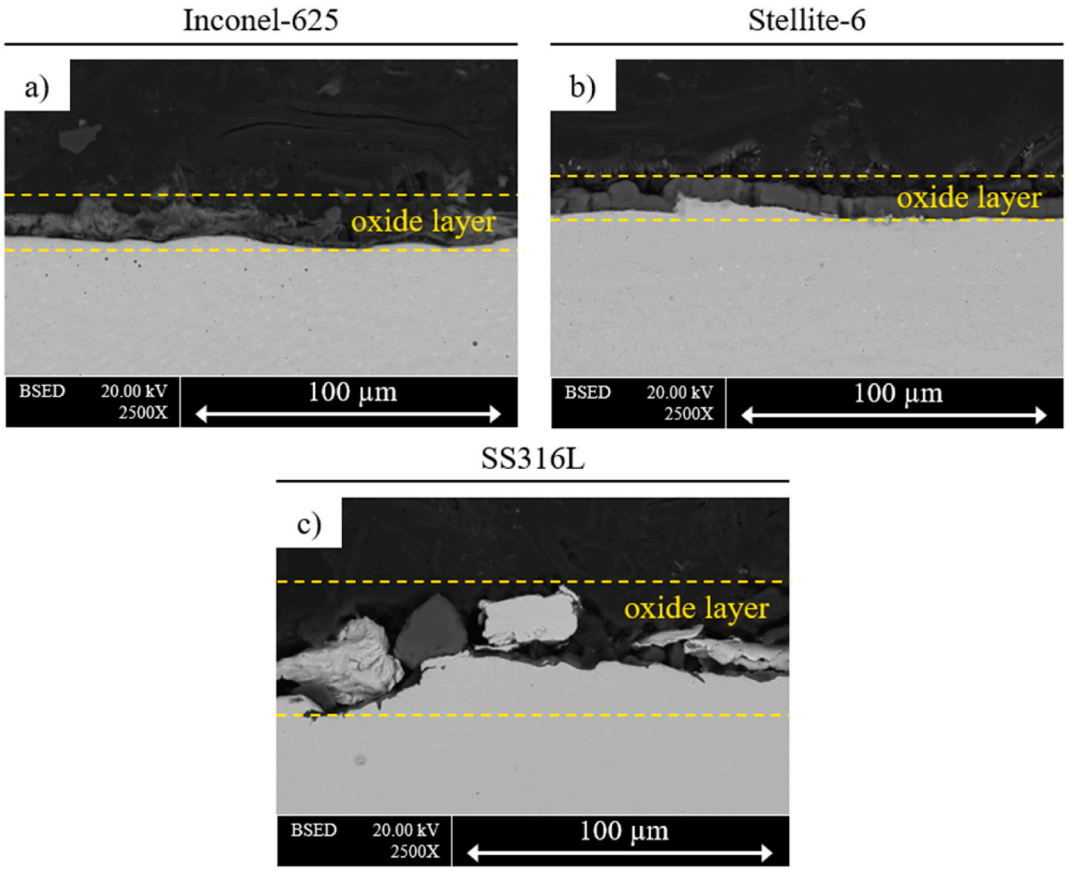

Fig. 6. SEM micrographs of cross-section of a) Inconel-625, b) Stellite-6, and c) SS316L samples after 3 months of immersion in molten salt-based nanofluids (2500X, 20 kV).

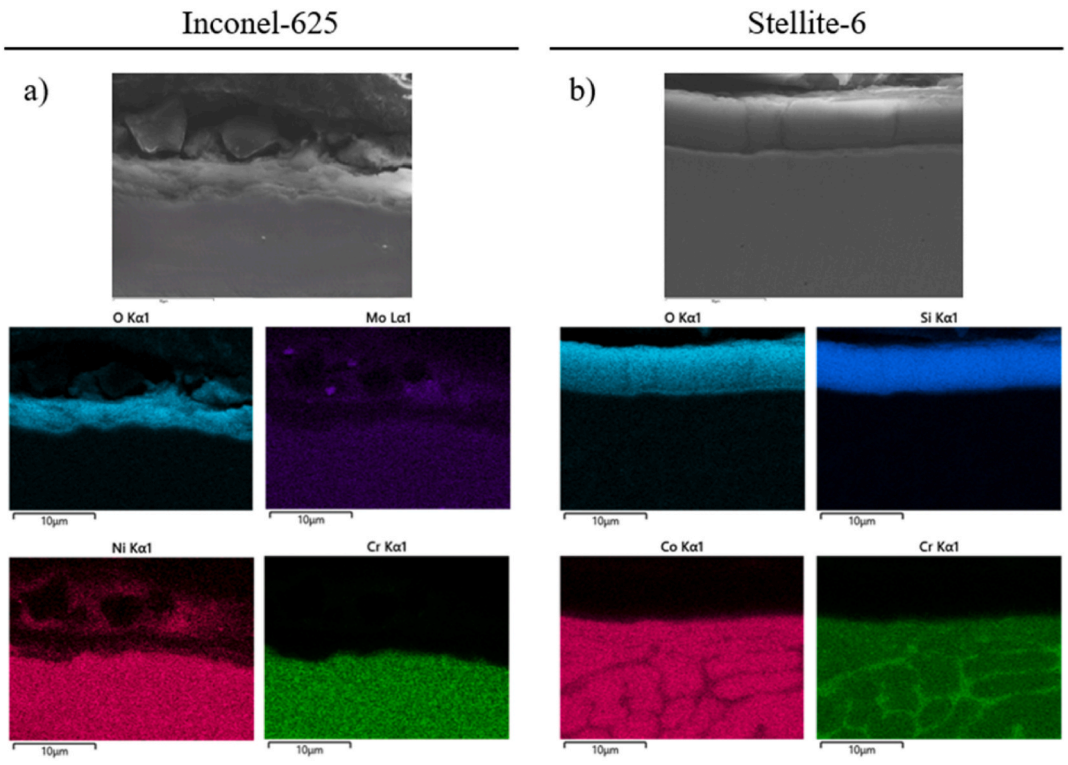

Fig. 7. Mapping of the cross-section of a) Inconel-625 and b) Stellite-6 samples after 3 months of immersion in molten salt-based nanofluids.

uniformity was corroborated by microscopical analysis of cross-sections, where homogeneous corrosion layers were observed across the surface of the specimens, with no evidence of severe localised attacks. These findings indicate that thickness loss measurement is an appropriate and representative method for evaluating corrosion in this study, as it accurately reflects the degree of material degradation across the entire exposed area. However, in scenarios where localised corrosion occurs, it would be necessary to supplement the evaluation with additional techniques, such as mass loss.

Moreover, the free surface analysis allowed a better study of the compounds formed after the test. Inconel-625 was composed of a mixture of elements (Fig. 8-a) present in the coating powder, such as nickel (Ni), chromium (Cr), iron (Fe), and molybdenum (Mo), elements in proportions lower than 1% that could be caused by the presence of impurities in the salts (Chlorine and sulphur, Cl and S) and elements such as sodium (Na) and silicon (Si) due to nanofluids. Similarly, the presence of O was observed, indicating that the layer formed is a mixture of oxides of the metals mentioned above. These compounds originate due to the spontaneous reaction of the solid phase metals (Nickel [Ni], chromium [Cr}, and molybdenum [Mo]) with the sodium nitrate ($NaNO_3$) molten salt (Equations (4)–(6)). These reactions are highly favoured due to negative values of the Gibbs free energy, $\Delta_r G_m^{\Theta}(T)$, between 600 K (327 °C) and 1000 K (727 °C) [66].

$$3Ni_{(s)} + 2NaNO_{3(l)} \leftrightarrow NiO_{(s)} + 2NO_{(g)} + Na_2O_{(s)}\ \Delta_r G_m^{\Theta}(600\text{-}1000\ K) = \text{-}189.05 \text{ to } \text{-}256.84\ kJ/mol \quad (4)$$

$$2Cr_{(s)} + 2NaNO_{3(l)} \leftrightarrow Cr_2O_{3(s)} + 2NO_{(g)} + Na_2O_{(s)}\ \Delta_r G_m^{\Theta}(600\text{-}1000\ K) = \text{-}615.37 \text{ to } \text{-}685.40\ kJ/mol \quad (5)$$

$$Mo_{(s)} + 2NaNO_{3(l)} \leftrightarrow Na_2MoO_{4(s)} + 2NO_{(g)}\ \Delta_r G_m^{\Theta}(600\text{-}1000\ K) = \text{-}537.43 \text{ to } \text{-}622.35\ kJ/mol \quad (6)$$

Stellite-6 as the mapping showed, this uniform layer (Fig. 8-b) was mainly composed of silicon oxide for Stellite-6. Zones with a high carbon (C) content by weight and salt particles ($NaNO_3$) adhering to the surface also existed. Finally, for the substrate material, significant surface damage due to corrosion was observed (Fig. 8-c), which was already visible in the cross-sectional images. Again, the agglomeration of the nanoparticles over a large area of the surface was shown.

An XRD analysis of the samples was carried out to evaluate the compounds on the surface under the corrosion test. Powders and coatings were analysed before and after the corrosion test to compare possible phase changes. The results are shown in Fig. 9. For the Inconel-625 sample, no crystallographic changes between the powders and the coatings deposited by LC were observed. The X-Ray diffraction pattern in both cases consists of (nickel, chromium, iron - Ni, Cr, Fe) phases with a cubic structure, in agreement with the results obtained in other studies [67,68]. In the case of the sample subjected to the corrosion test, an additional cristobalite (SiO_2) phase with a tetragonal structure appeared due to the aggregation of nanoparticles on the surface of the sample. In the case of the Stellite-6 sample, the diffraction pattern was composed of peaks of (cobalt, chromium - Co, Cr) phases of cubic structure for both powder and coating. These results are in accordance with other studies [69,70] using the same coating. Cristobalite peaks also appear for the sample that was 90 days in the corrosion test. In addition to this, an additional sodium nitrate ($NaNO_3$) phase with rhombohedral structure appeared due to the adhesion of the molten salt on the sample.

Finally, the results obtained from the metal analysis of the salts (ICP), after the corrosion test, corroborated all of the mentioned above. In the molten salt-based nanofluid in contact with the Inconel-625 sample, amounts of 3.6 ± 0.3 µg/g nickel (Ni) and 6 ± 4 µg/g chromium (Cr) were found. This implied that most of the Ni tended to remain as an oxide in the surface layer of the sample, while the chromium (Cr) was transferred to the salt. This was already evident from the mapping, where almost no chromium (Cr) was observed in the oxide layer formed. The other metals studied for this sample were in negligible proportions. In contrast, for the sample in contact with Stellite-6, only 10 ± 1 µg/g chromium (Cr) was detected. This means that the chromium (Cr) present in the coating partly passed into the salt, instead of forming a surface

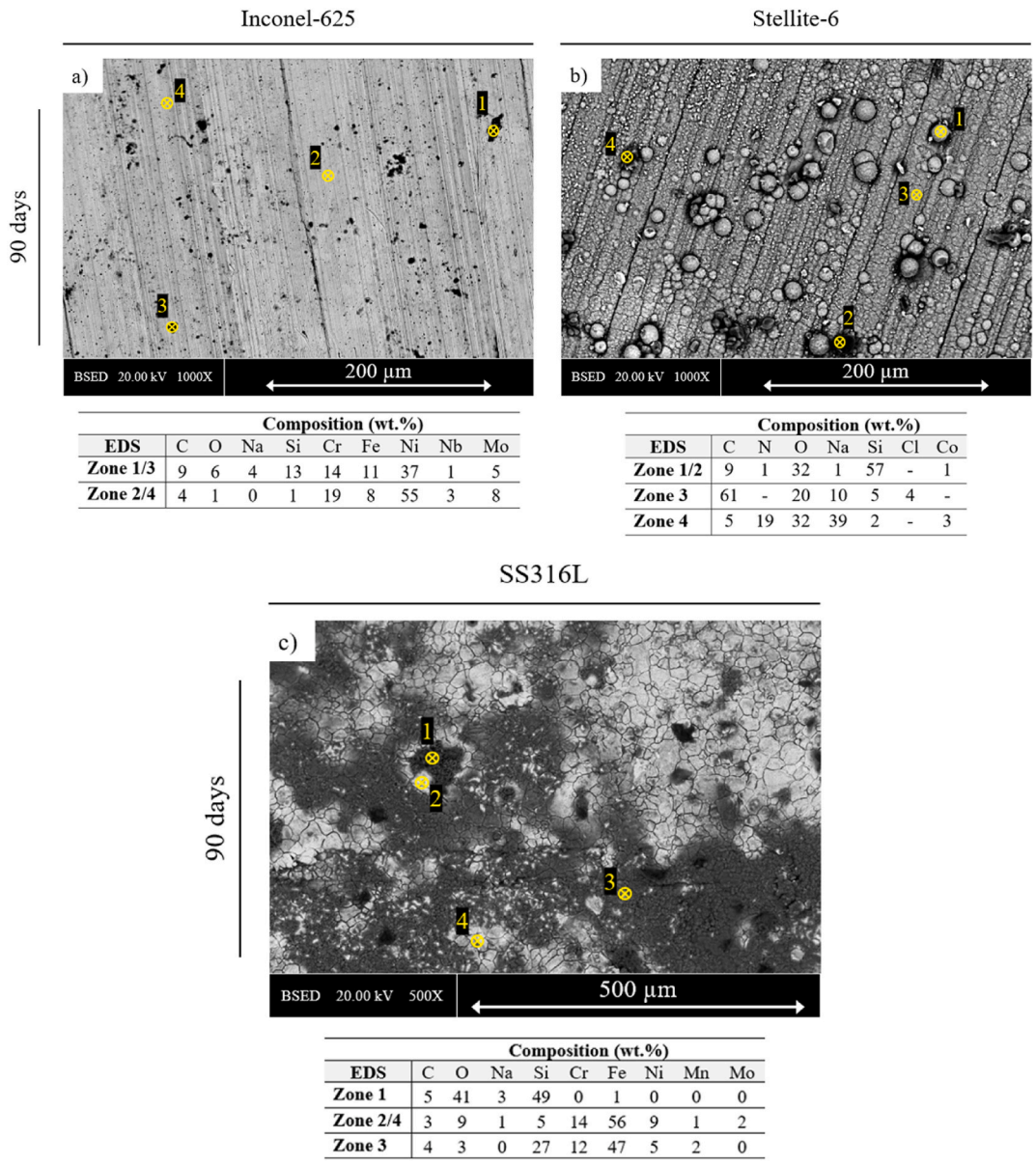

	Composition (wt.%)								
EDS	C	O	Na	Si	Cr	Fe	Ni	Nb	Mo
Zone 1/3	9	6	4	13	14	11	37	1	5
Zone 2/4	4	1	0	1	19	8	55	3	8

	Composition (wt.%)						
EDS	C	N	O	Na	Si	Cl	Co
Zone 1/2	9	1	32	1	57	-	1
Zone 3	61	-	20	10	5	4	-
Zone 4	5	19	32	39	2	-	3

	Composition (wt.%)								
EDS	C	O	Na	Si	Cr	Fe	Ni	Mn	Mo
Zone 1	5	41	3	49	0	1	0	0	0
Zone 2/4	3	9	1	5	14	56	9	1	2
Zone 3	4	3	0	27	12	47	5	2	0

Fig. 8. SEM micrographs of the free surface of a) Inconel-625, b) Stellite-6 and c) SS316L samples after 3 months of immersion in molten salt-based nanofluids and EDS analysis.

oxide layer. Moreover, the minimal presence of cobalt (Co) in this salt implies that there was no diffusion of this element between the coating and the salt, probably prevented by the layer of nanoparticles formed.

4. Conclusions

Based on the results obtained, both coatings showed excellent performance against corrosion in molten sodium nitrate ($NaNO_3$) with SiO_2 nanoparticles at 450 °C. This confirms that the use of this type of coating material improves the resistance of TES tanks and increases their service life. The most relevant points are described below.

- None of the coated samples showed significant signs of surface corrosion. This was mainly due to the compact and uniform coatings with thicknesses that provided effective protection against the nanofluids' corrosive behaviour. Furthermore, thickness reductions were minimal, reaching values of 30.2 ± 6 µm for Inconel-625 and 26.9 ± 10 µm for Stellite-6. This resulted in 122.5 ± 24 µm/year corrosion rates for Inconel-625 and 109.2 ± 40 µm/year for Stellite-6. In comparison, 316L stainless steel showed a significantly higher corrosion rate of 240 ± 24 µm/year.
- Surface analysis of the samples revealed the formation of an oxide layer. In the case of Stellite-6, a solid and homogeneous silicon oxide (SiO_2) layer was formed. This layer could have acted as a protective barrier, slowing down the coating's corrosion process. However, further research will be necessary to corroborate this relationship.
- XRD analysis showed no significant phase changes upon deposition of the coatings. Furthermore, it allowed to observe the appearance of additional phases, such as cristobalite, due to the agglomeration of the silicon oxide (SiO_2) nanoparticles on the sample surface.
- Metal analysis showed the diffusion of elements such as nickel (Ni) and chromium (Cr) into the salt. However, future tests on the salts will be necessary to determine how this affects their thermal properties.
- The experimental results are promising for TES tanks in the field of CSP plants, although more studies are needed with longer test times and a greater variety of salts.

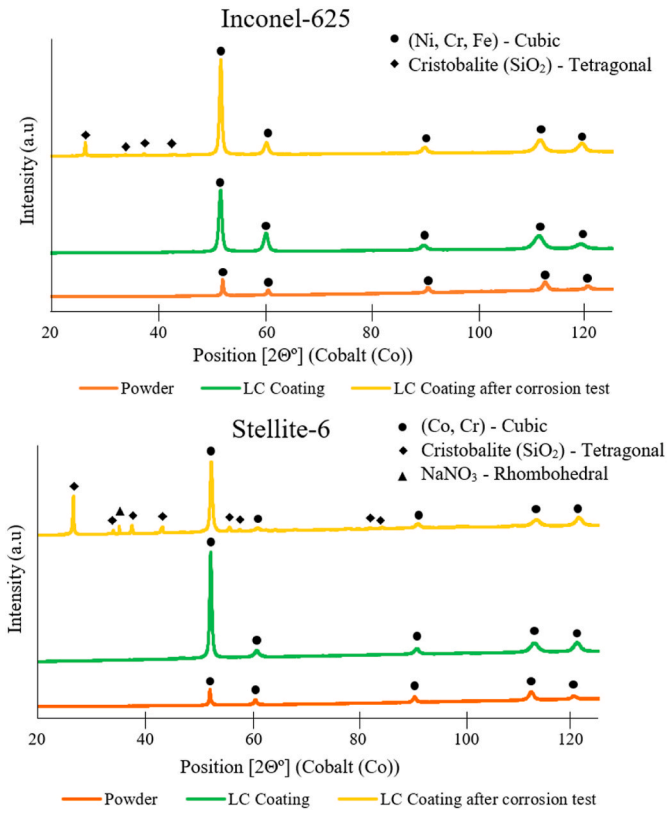

Fig. 9. XRD of a) Inconel-625 and b) Stellite-6 samples (powder (orange line), LC coating (green line), and LC coating after corrosion test (yellow line).

Declaration of competing interest

The authors declare that they have no known competing financial interests or personal relationships that could have appeared to influence the work reported in this paper.

Acknowledgments

The authors would like to thank the Catalan Government for the quality accreditation given to their research group DIOPMA (2021 SGR 00708 and 2021 SGR 00512). DIOPMA is a certified agent TECNIO in the category of technology developers from the Government of Catalonia. This work has been partially funded by the Spanish government PID2021-123511OB-C32 (MICINN/FEDER, UE) and supported by "100 Foreign Experts Plan of Hebei Province". This work couldn't be carried out without the support of "Thermodust" project (n. 101046835) funded by the "Horizon Europe" framework programme, and also CDTI and NextGeneration EU funds for the Bioenergy project MIP-20221004. Additionally, A special thanks to TM COMAS SLU company, which supported the project by providing the coating samples for testing.

References

[1] Yolcan OO. World energy outlook and state of renewable energy: 10-year evaluation. Innov Green Dev 2023;2:100070. https://doi.org/10.1016/j.igd.2023.100070.
[2] Sayed E, Olabi A, Alami A, Radwan A, Mdallal A, Rezk A, et al. Renewable energy and energy storage systems. Energies 2023;16:1415. https://doi.org/10.3390/en16031415.
[3] Jabarov SH, Huseynov RE, Ayyubova GSh, Trukhanov SV, Trukhanov AV, Aliyev YI, et al. Evaluation of structural characteristics BaFe(12-x)InxO19 hexaferrite compounds at high temperatures. Solid State Commun 2024;386:115529. https://doi.org/10.1016/j.ssc.2024.115529.
[4] Storage Innovations. EnergyGov n.d. https://www.energy.gov/oe/storage-innovations-2030. [Accessed 9 July 2024].
[5] Innovation outlook: thermal energy storage. Abu Dhabi: IRENA, International Renewable Energy Agency; 2020.
[6] Dosta S, Betancor L, Barreneche C. Overview of surface engineering technology to improve the energy efficiency in concentrated solar power (CSP) plants. Sol Energy Mater Sol Cells 2024;277:113090. https://doi.org/10.1016/j.solmat.2024.113090.
[7] Achkari O, El Fadar A. Latest developments on TES and CSP technologies – energy and environmental issues, applications and research trends. Appl Therm Eng 2020;167:114806. https://doi.org/10.1016/j.applthermaleng.2019.114806.
[8] Bauer T, Odenthal C, Bonk A. Molten salt storage for power generation. Chem Ing Tech 2021;93:534–46. https://doi.org/10.1002/cite.202000137.
[9] Zhang HL, Baeyens J, Degrève J, Cacères G. Concentrated solar power plants: review and design methodology. Renew Sustain Energy Rev 2013;22:466–81. https://doi.org/10.1016/j.rser.2013.01.032.
[10] Walczak M, Pineda F, Fernández ÁG, Mata-Torres C, Escobar RA. Materials corrosion for thermal energy storage systems in concentrated solar power plants. Renew Sustain Energy Rev 2018;86:22–44. https://doi.org/10.1016/j.rser.2018.01.010.
[11] Prieto C, Ruiz-Cabañas J, Madina V, Fernández AI, Cabeza LF. Lessons learned from corrosion of materials with molten salts during molten salt tank preheating. Sol Energy Mater Sol Cells 2022;247:111943. https://doi.org/10.1016/j.solmat.2022.111943.
[12] Osorio J, Mehos M, Imponenti L, Kelly B, Price H, Torres-Madronero J, et al. Failure analysis for molten salt thermal energy storage tanks for In-Service CSP plants. https://doi.org/10.2172/2331241; 2024.
[13] Chen X, Zhang M, Wu Y, Ma C. Advances in high-temperature molten salt-based carbon nanofluid research. Energies 2023;16:2178. https://doi.org/10.3390/en16052178.
[14] Pereira J, Moita A, Moreira A. An overview of the molten salt nanofluids as thermal energy storage media. Energies 2023;16:1825. https://doi.org/10.3390/en16041825.
[15] Pordanjani AH, Aghakhani S, Afrand M, Sharifpur M, Meyer JP, Xu H, et al. Nanofluids: physical phenomena, applications in thermal systems and the environment effects- a critical review. J Clean Prod 2021;320:128573. https://doi.org/10.1016/j.jclepro.2021.128573.
[16] Muñoz-Sánchez B, Nieto-Maestre J, Iparraguirre-Torres I, García-Romero A, Sala-Lizarraga JM. Molten salt-based nanofluids as efficient heat transfer and storage materials at high temperatures. An overview of the literature. Renew Sustain Energy Rev 2018;82:3924–45. https://doi.org/10.1016/j.rser.2017.10.080.
[17] Muñoz-Sánchez B, Nieto-Maestre J, Guerreiro L, Julia JE, Collares-Pereira M, García-Romero A. Molten salt based nanofluids based on solar salt and alumina nanoparticles: an industrial approach. Abu Dhabi, United Arab Emirates, https://doi.org/10.1063/1.4984437; 2017.
[18] Wang W, Wu Z, Li B, Sundén B. A review on molten-salt-based and ionic-liquid-based nanofluids for medium-to-high temperature heat transfer. J Therm Anal Calorim 2019;136:1037–51. https://doi.org/10.1007/s10973-018-7765-y.
[19] Tiznobaik H, Shin D. Enhanced specific heat capacity of high-temperature molten salt-based nanofluids. Int J Heat Mass Tran 2013;57:542–8. https://doi.org/10.1016/j.ijheatmasstransfer.2012.10.062.
[20] Dunham MT, Iverson BD. High-efficiency thermodynamic power cycles for concentrated solar power systems. Renew Sustain Energy Rev 2014;30:758–70. https://doi.org/10.1016/j.rser.2013.11.010.
[21] Svobodova-Sedlackova A, Palacios A, Jiang Z, Renna AIF, Ding Y, Navarro H, et al. Thermal stability and durability of solar salt-based nanofluids in concentrated solar power thermal energy storage: an approach from the effect of diverse metal alloys corrosion. J Energy Storage 2024;75:109715. https://doi.org/10.1016/j.est.2023.109715.
[22] Nithiyanantham U, Grosu Y, González-Fernández L, Zaki A, Igartua JM, Faik A. Corrosion aspects of molten nitrate salt-based nanofluids for thermal energy storage applications. Sol Energy 2019;189:219–27. https://doi.org/10.1016/j.solener.2019.07.050.
[23] Navarro ME, Palacios A, Jiang Z, Avila A, Qiao G, Mura E, et al. Effect of SiO2 nanoparticles concentration on the corrosion behaviour of solar salt-based nanofluids for concentrating solar power plants. Sol Energy Mater Sol Cells 2022;247:111923. https://doi.org/10.1016/j.solmat.2022.111923.
[24] Katayama S. Handbook of laser welding technologies. 2013.
[25] Zhu L, Xue P, Lan Q, Meng G, Ren Y, Yang Z, et al. Recent research and development status of laser cladding: a review. Opt Laser Technol 2021;138:106915. https://doi.org/10.1016/j.optlastec.2021.106915.
[26] Seraj RA, Abdollah-zadeh A, Dosta S, Canales H, Assadi H, Cano IG. The effect of traverse speed on deposition efficiency of cold sprayed stellite 21. Surf Coat Technol 2019;366:24–34. https://doi.org/10.1016/j.surfcoat.2019.03.012.
[27] Lester S, Longfield N, Griffiths J, Cocker J, Staudenmaier C, Broadhead G. New systems for laser cladding: Laser surface modifications in steel industry. Laser Technol J 2013;10:41–3. https://doi.org/10.1002/latj.201390037.
[28] Rezayat M, Aboutorabi Sani A, Talafi Noghani M, Saghafi Yazdi M, Taheri M, Moghanian A, et al. Effect of lateral laser-cladding process on the corrosion performance of inconel 625. Metals 2023;13:367. https://doi.org/10.3390/met13020367.
[29] Abe F, Osakada K, Shiomi M, Uematsu K, Matsumoto M. The manufacturing of hard tools from metallic powders by selective laser melting. J Mater Process Technol 2001;111:210–3. https://doi.org/10.1016/S0924-0136(01)00522-2.
[30] Lima CRC, Dosta S, Guilemany JM, Clarke DR. The application of photoluminescence piezospectroscopy for residual stresses measurement in thermally sprayed TBCs. Surf Coat Technol 2017;318:147–56. https://doi.org/10.1016/j.surfcoat.2016.07.084.

[31] Scendo M, Staszewska-Samson K, Danielewski H. Corrosion behavior of inconel 625 coating produced by laser cladding. Coatings 2021;11:759. https://doi.org/10.3390/coatings11070759.
[32] Smolina I, Kobiela K. Characterization of wear and corrosion resistance of stellite 6 laser surfaced alloyed (LSA) with rhenium. Coatings 2021;11:292. https://doi.org/10.3390/coatings11030292.
[33] Sidhu BS, Prakash S. Studies on the behaviour of stellite-6 as plasma sprayed and laser remelted coatings in molten salt environment at 900°C under cyclic conditions. J Mater Process Technol 2006;172:52–63. https://doi.org/10.1016/j.jmatprotec.2005.08.018.
[34] Cinca N, López E, Dosta S, Guilemany JM. Study of stellite-6 deposition by cold gas spraying. Surf Coat Technol 2013;232:891–8. https://doi.org/10.1016/j.surfcoat.2013.06.120.
[35] Dosta S, Cinca N, Silvello A, Cano IG. Alumina reinforcement of inconel 625 coatings by cold gas spraying. Metals 2020;10:1263. https://doi.org/10.3390/met10091263.
[36] Seraj RA, Abdollah-zadeh A, Dosta S, Assadi H, Cano IG. Comparison of stellite coatings on low carbon steel produced by CGS and HVOF spraying. Surf Coat Technol 2019;372:299–311. https://doi.org/10.1016/j.surfcoat.2019.05.022.
[37] Abioye TE, McCartney DG, Clare AT. Laser cladding of inconel 625 wire for corrosion protection. J Mater Process Technol 2015;217:232–40. https://doi.org/10.1016/j.jmatprotec.2014.10.024.
[38] Yang Z, Jian Y, Chen Z, Qi H, Huang Z, Huang G, et al. Microstructure, hardness and slurry erosion-wear behaviors of high-speed laser cladding Stellite 6 coatings prepared by the inside-beam powder feeding method. J Mater Res Technol 2022;19:2596–610. https://doi.org/10.1016/j.jmrt.2022.06.025.
[39] Bartkowski D, Młynarczak A, Piasecki A, Dudziak B, Gościański M, Bartkowska A. Microstructure, microhardness and corrosion resistance of Stellite-6 coatings reinforced with WC particles using laser cladding. Opt Laser Technol 2015;68:191–201. https://doi.org/10.1016/j.optlastec.2014.12.005.
[40] Soleimani Dorcheh A, Durham RN, Galetz MC. Corrosion behavior of stainless and low-chromium steels and IN625 in molten nitrate salts at 600 °C. Sol Energy Mater Sol Cells 2016;144:109–16. https://doi.org/10.1016/j.solmat.2015.08.011.
[41] Prem Kumar M, Manikandan M. Insights into the surface behavior of Inconel 617 and Inconel 625 material in molten salt. Mater Lett 2023;333:133679. https://doi.org/10.1016/j.matlet.2022.133679.
[42] Sidhu BS, Prakash S. Performance of NiCrAlY, Ni–Cr, Stellite-6 and Ni3Al coatings in Na2SO4–60% V2O5 environment at 900°C under cyclic conditions. Surf Coat Technol 2006;201:1643–54. https://doi.org/10.1016/j.surfcoat.2006.02.035.
[43] Sidhu TS, Prakash S, Agrawal RD. Evaluation of hot corrosion resistance of HVOF coatings on a Ni-based superalloy in molten salt environment. Mater Sci Eng, A 2006;430:64–78. https://doi.org/10.1016/j.msea.2006.05.099.
[44] Prashar G, Vasudev H. Hot corrosion behavior of super alloys. Mater Today Proc 2020;26:1131–5. https://doi.org/10.1016/j.matpr.2020.02.226.
[45] C09 Committee. Practice for reducing samples of aggregate to testing size n.d. https://doi.org/10.1520/C0702_C0702M-11.
[46] Svobodova-Sedlackova A, Barreneche C, Gamallo P, Fernández AI. Novel sampling procedure and statistical analysis for the thermal characterization of ionic nanofluids. J Mol Liq 2022;347:118316. https://doi.org/10.1016/j.molliq.2021.118316.
[47] Moore R, Siegel N, Kolb G, Vernon M, Ho C. Design considerations for concentrating solar power tower systems employing molten salt. https://doi.org/10.2172/1008140; 2010.
[48] Liu J, Li L. Effects of process variables on laser direct formation of thin wall. Opt Laser Technol 2007;39:231–6. https://doi.org/10.1016/j.optlastec.2005.08.012.
[49] Zhou S, Zeng X, Hu Q, Huang Y. Analysis of crack behavior for Ni-based WC composite coatings by laser cladding and crack-free realization. Appl Surf Sci 2008;255:1646–53. https://doi.org/10.1016/j.apsusc.2008.04.003.
[50] Gomes A, Navas M, Uranga N, Paiva T, Figueira I, Diamantino TC. High-temperature corrosion performance of austenitic stainless steels type AISI 316L and AISI 321H, in molten solar salt. Sol Energy 2019;177:408–19. https://doi.org/10.1016/j.solener.2018.11.019.
[51] Sutter F, Oskay C, Galetz MC, Diamantino T, Pedrosa F, Figueira I, et al. Dynamic corrosion testing of metals in solar salt for concentrated solar power. Sol Energy Mater Sol Cells 2021;232:111331. https://doi.org/10.1016/j.solmat.2021.111331.
[52] Swaminathan S, Kumar S, Kranzmann A, Hesse R, Goldbeck H, Fantin A. Corrosion characteristics of 316L stainless steel in oxide-rich molten solar salt at 600 °C. Sol Energy Mater Sol Cells 2024;278:113176. https://doi.org/10.1016/j.solmat.2024.113176.
[53] Lai X, Yin H, Yang Z, Tang Z. Synergistic effect of Cl− and F− on the corrosion behavior and mechanism of 316 stainless steel in NaNO3-based molten salts and vapor. J Energy Storage 2023;65:107243. https://doi.org/10.1016/j.est.2023.107243.
[54] Sandoval-Amador A, Santander-Vega AJ, Amaya-Cáceres CC, Estupiñán-Duran HA, Peña-Ballesteros DY. 316L stainless steel corrosion in molten salts NaNO3 KNO3 NaNO2 simulating storage conditions. J Phys, Conf Ser 2019;1159:012011. https://doi.org/10.1088/1742-6596/1159/1/012011.
[55] Kruizenga AM, Gill DD, LaFord ME. Materials corrosion of high temperature alloys immersed in 600C binary nitrate salt. Livermore, CA (United States): Sandia National Lab. (SNL-CA); 2013. https://doi.org/10.2172/1088090.
[56] Su Y, Li H, Yang T, Dai Z, Zhang G. Study on the corrosion behavior of inconel 625 deposited metal against molten nitrate. Mater Today Commun 2024;40:109699. https://doi.org/10.1016/j.mtcomm.2024.109699.
[57] Naghiyan Fesharaki M, Shoja-Razavi R, Mansouri HA, Jamali H. Evaluation of the hot corrosion behavior of Inconel 625 coatings on the Inconel 738 substrate by laser and TIG cladding techniques. Opt Laser Technol 2019;111:744–53. https://doi.org/10.1016/j.optlastec.2018.09.011.
[58] Wang X, Fu K, Ren X, Xue Y, Luan B. Investigation on the high-temperature molten salt corrosion properties of the Inconel 625 coatings prepared on Q245R steel by high-speed laser cladding. Surf Interfaces 2025;72:107190. https://doi.org/10.1016/j.surfin.2025.107190.
[59] Yao J, Ding Y, Liu R, Zhang Q, Wang L. Wear and corrosion performance of laser-clad low-carbon high-molybdenum Stellite alloys. Opt Laser Technol 2018;107:32–45. https://doi.org/10.1016/j.optlastec.2018.05.021.
[60] Jeyaprakash N, Yang C-H, Karuppasamy SS, Dhineshkumar SR. Evaluation of microstructure, nanoindentation and corrosion behavior of laser cladded Stellite-6 alloy on Inconel-625 substrate. Mater Today Commun 2022;31:103370. https://doi.org/10.1016/j.mtcomm.2022.103370.
[61] Rosalbino F, Scavino G. Corrosion behaviour assessment of cast and HIPed Stellite 6 alloy in a chloride-containing environment. Electrochim Acta 2013;111:656–62. https://doi.org/10.1016/j.electacta.2013.08.019.
[62] Palacios A, Navarro ME, Jiang Z, Avila A, Qiao G, Mura E, et al. High-temperature corrosion behaviour of metal alloys in commercial molten salts. Sol Energy 2020;201:437–52. https://doi.org/10.1016/j.solener.2020.03.010.
[63] Prieto C, Blindu A, Cabeza LF, Valverde J, García G. Molten salts tanks thermal energy storage: aspects to consider during design. Energies 2023;17:22. https://doi.org/10.3390/en17010022.
[64] Česánek Z, Houdková Š, Lukáč F. High-temperature corrosion behavior of selected thermally sprayed coatings in corrosive aggressive environment. Mater Res Express 2019;6. https://doi.org/10.1088/2053-1591/aae956.
[65] Ma L, Zhang C, Wu Y, Lu Y. Effect of flow rate and SiO2 nanoparticle on dynamic corrosion behavior of stainless steels in molten salt for thermal energy storage. Corros Sci 2022;194:109952. https://doi.org/10.1016/j.corsci.2021.109952.
[66] Yang C, Wei X, Peng Q, Ding J, Yang J. Effect of nickel base alloy on NO x emissions from binary molten nitrate salts in thermal energy storage process. Energy Proc 2017;105:4003–8. https://doi.org/10.1016/j.egypro.2017.03.837.
[67] Han D, Hou Y, Jiang B, Geng B, He X, Shagdar E, et al. Enhanced corrosion resistance of alloy in molten chloride salts by adding nanoparticles for thermal energy storage applications. J Energy Storage 2023;64:107172. https://doi.org/10.1016/j.est.2023.107172.
[68] Feng K, Chen Y, Deng P, Li Y, Zhao H, Lu F, et al. Improved high-temperature hardness and wear resistance of Inconel 625 coatings fabricated by laser cladding. J Mater Process Technol 2017;243:82–91. https://doi.org/10.1016/j.jmatprotec.2016.12.001.
[69] Houdková Š, Pala Z, Smazalová E, Vostřák M, Česánek Z. Microstructure and sliding wear properties of HVOF sprayed, laser remelted and laser clad Stellite 6 coatings. Surf Coat Technol 2017;318:129–41. https://doi.org/10.1016/j.surfcoat.2016.09.012.
[70] Luo F, Cockburn A, Lupoi R, Sparkes M, O'Neill W. Performance comparison of Stellite 6® deposited on steel using supersonic laser deposition and laser cladding. Surf Coat Technol 2012;212:119–27. https://doi.org/10.1016/j.surfcoat.2012.09.031.